Heliyon 9 (2023) e21117

Contents lists available at ScienceDirect

Heliyon

journal homepage: www.cell.com/heliyon

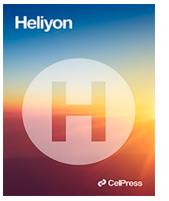

Review article

Advances in thermoelectric $AgBiSe_2$: Properties, strategies, and future challenges

Hanhwi Jang [a], Yeon Sik Jung [a], Min-Wook Oh [b,*]

[a] Department of Materials Science and Engineering, Korea Advanced Institute of Science and Technology (KAIST), Daejeon, 34141, Republic of Korea

[b] Department of Materials Science and Engineering, Hanbat National University, Yuseong-gu, Daejeon, 34158, Republic of Korea

A B S T R A C T

Thermoelectric materials are attracting considerable attention to alleviate the global energy crisis by enabling the direct conversion of heat into electricity. As a class of I–V–VI_2 semiconductors, $AgBiSe_2$ is expected to be the potential thermoelectric material to replace conventional PbTe-based compounds due to its non-toxic and abundant nature of its constituent elements. This review article summarizes the fundamental properties of $AgBiSe_2$, thermoelectric properties, the effect of different dopants on its transport properties and entropy engineering for cubic phase stabilization with the detailed description of related techniques used to analyze the properties of $AgBiSe_2$. The current thermoelectric figure-of-merit and approaches to further improve performance and operational stability are also discussed.

1. Introduction

The limitation of fossil fuel consumption and the efficient utilization of heat as a practical form of energy have been called for in an effort to alleviate the energy crisis that the world is currently facing [1–3]. Therefore, a solid-state device that can convert heat into electrical energy - namely, a thermoelectric generator (TEG) -has attracted a considerable attention as a promising technology for a sustainable future [4–6]. Compared to other waste heat recovery techniques (e.g., heat pumps and steam generators), TEGs have several advantages stemming from an absence of mechanical moving parts: a silent operation without noise, long-term durability, and compactness of the device [7,8]. Nevertheless, the commercialization and related market growth of TEG technologies have been stagnating for a while due to the poor energy conversion efficiency of TE modules [9,10]. Generally, a conversion efficiency of the TE module is proportional to the dimensionless TE figure-of-merit (zT), which is given by $zT = S^2\sigma T/\kappa$, where S, σ, T, and κ are the Seebeck coefficient, electrical conductivity, absolute temperature, and total thermal conductivity of a TE material [11–13]. However, increasing the zT of a TE material has been extremely complicated by an interplay of each parameter; for example, improving σ by increasing a carrier concentration would increase κ and decrease S [14,15].

For decades, several narrow-gap semiconductors have been investigated as promising thermoelectric materials. For example, Bi_2Te_3 [10,16–18], $CoSb_3$ [19–22], SnSe [23–27], PbTe [12,28–32], Mg_3Sb_2 [33–37], and $AgSbTe_2$ [38–40] have exhibited superior TE properties compared to other classes of materials. Although mostly p-type, GeTe-based materials also exhibit superior TE performance with zT near 2.0 at 700 K [41–43]. SnSe-based materials have ultrahigh zT values in both n- and p-type samples [24,25,44]. However, the structural transition of GeTe can cause significant volume change and lead to device failure during operation [45], while the high TE performance of SnSe is often limited to single-crystal samples only [46]. For the stable operation with high TE performance, lead telluride (PbTe)-based materials have been adopted due to their superior TE properties (e.g., intrinsically low thermal

* Corresponding author.
E-mail address: mwoh@hanbat.ac.kr (M.-W. Oh).

https://doi.org/10.1016/j.heliyon.2023.e21117
Received 17 July 2023; Received in revised form 4 October 2023; Accepted 16 October 2023
Available online 18 October 2023

conductivity and high electrical conductivity). However, an alternative to PbTe has been necessary considering the toxicity of Pb and the related environmental regulations. Under these circumstances, divalent Pb can be replaced by a combination of monovalent group 11 elements and trivalent group 13 elements, where ABX_2 compounds (A = Cu, Ag, Au; B═Sb, Bi, X = S, Se, Te) have been emerged as prospective TE material candidates. These compounds are known to exhibit ultralow lattice thermal conductivity due to the presence of lone-pair electrons in the B-site cations [47,48] and the formation of spontaneous nanostructures [49]. As a result, ABX_2 compounds have been considered an intriguing candidate for high performance TE materials.

Among several ABX_2 compounds, the low abundance of Te in the Earth's crust has led to the development of selenides [50]. Moreover, when the A-site is occupied by Ag, the lattice thermal conductivity becomes significantly lower compared to the case where the A-site is occupied by Cu [51]. Therefore, $AgSbSe_2$ and $AgBiSe_2$ serve as an attractive alternative to the conventional PbTe-based TE materials. In this review, we will focus on silver bismuth diselenide ($AgBiSe_2$)-based TE materials, one of the representative ABX_2 compounds with interesting temperature-dependent polymorphism and unconventional transport properties. TE properties of pure $AgBiSe_2$ and some doping strategies to tune the properties are presented, including cubic phase stabilization and related defect chemistry of $AgBiSe_2$. Finally, remaining challenges for the practical application of $AgBiSe_2$ as an energy harvesting device and future prospects for further improving TE properties of $AgBiSe_2$ are discussed.

2. Properties of pure $AgBiSe_2$

2.1. Crystal structure

The crystallographic information of $AgBiSe_2$ was first reported by Geller et al. in 1959 [52] and detailed characterization was performed after the mineral "Bohdanowiczite" is reported by Banas et al. in 1967 [53]. As shown in Fig. 1a, it crystallizes to the trigonal structure (space group *P*-3*m*1) with characteristic Se–Ag–Se–Bi–Se–Ag–Se–Bi–Se–Ag–Se chains separated by metallic Bi atoms. With an increase in temperature to 510 K, the Bi–Se bonds are weakened, resulting in a slight distortion of the unit cell to the rhombohedral structure. Since the volume change during this phase transition is marginal, the transition enthalpy is measured to be small when analyzed by differential scanning calorimetry (DSC). Xiao et al. evaluated a change in bonding environment during this phase transition [54]. In the trigonal structure, there are two crystallographic sites available for Bi atoms: one for Bi^{3+} having a bond length of 2.993 and 2.981 Å, while metallic Bi has a bond length of 3.04 Å, presumably due to a weaker bonding from an absence of electron transfer (Fig. 1b). During the rhombohedral transition, however, the chemical environment of two Bi atoms becomes equivalent with the same Bi–Se bond length of 3.032 Å. Further increase in the temperature to 580 K promotes a rhombohedral to cubic transition with a possible disordering of Ag and Bi atoms, which will be discussed later. The crystallographic information and physical

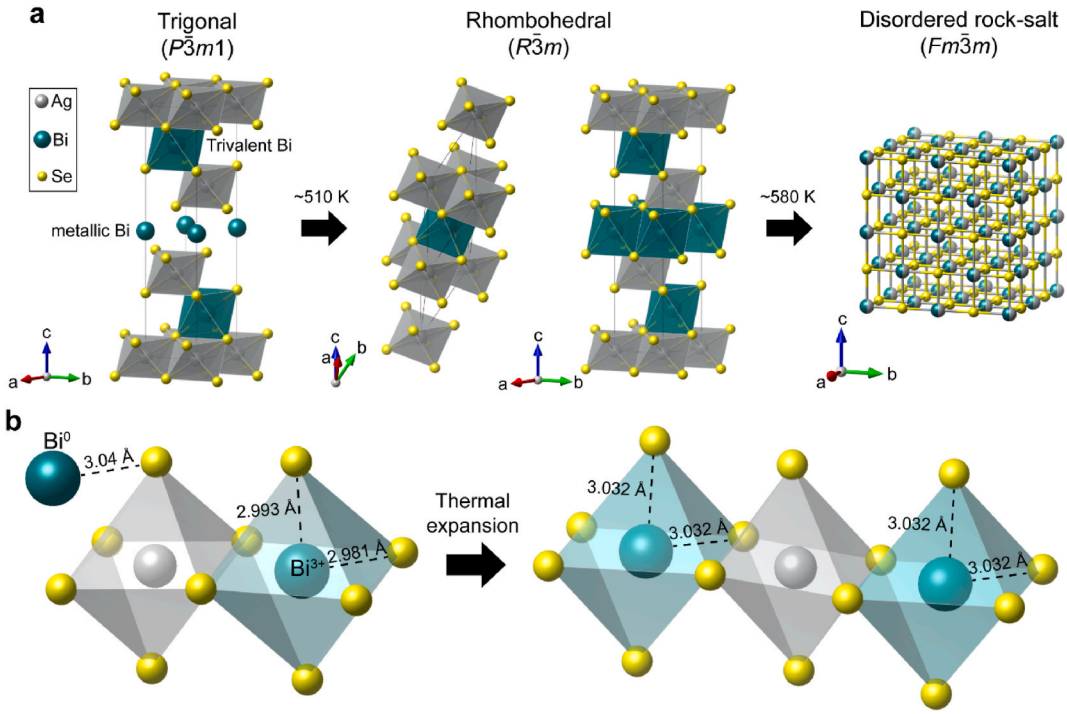

Fig. 1. Crystal structure and polymorphism of $AgBiSe_2$. (a) $AgBiSe_2$ crystallizes into a trigonal structure at room temperature and undergoes two phase transitions upon heating. The Trigonal to rhombohedral and rhombohedral to cubic transition occur at around 510 and 580 K, respectively. (b) Change in Bi–Se bond length during the trigonal to rhombohedral transition.

properties of trigonal $AgBiSe_2$ are summarized in Table 1.

2.2. Cation configuration and electronic properties

The cation configuration of cubic $AgBiSe_2$ and other ABX_2 compounds has been complicated because the conventional powder X-ray diffraction technique may not be an ideal tool to reveal the local environment of a material. However, using the density functional theory (DFT) calculations, it has been found that ordered cation configurations are energetically favored over the disordered structure [55]. Hoang et al. estimated the formation energy of cation-ordered $AgSbTe_2$ using DFT calculations, and found that the AF-II and AF-IIb are the most stable structures (Fig. 2a). Careful single crystal X-ray diffraction experiments also confirmed the existence of cation ordering in $AgSbTe_2$ [56]. The observations on the cation ordering of ABX_2 compounds are important because the cation configuration can significantly affect to the electronic band structure of a compound. Fig. 2b shows a change in the electronic density-of-states (DOS) and variation of the pseudogap feature by the cation configuration in $AgSbTe_2$. Hoang et al. found that the presence of Ag in Sb–Te–Sb–Te– … chains strongly perturbs the hybridization between Sb and Te, leading to the development of a pseudogap in the AF-II and AF-IIb structure [55].

Similarly, cubic $AgBiSe_2$ is expected to exhibit cation ordering according to the DFT calculations of Xiao et al. where AF-II and AF-IIb are the most preferred configurations among possible structures [54]. However, experimental observation of cation ordering in $AgBiSe_2$ has been obscured by the limited thermodynamic stability of cubic $AgBiSe_2$ at room temperature, which exists only at temperatures above 580 K. Manolikas et al. performed transmission electron microscopy (TEM) of cubic $AgBiSe_2$ by quenching the sample from a high temperature [57]. However, selected area electron diffraction (SAED) pattern of the quenched sample showed no evidence of cation ordering. Neutron diffuse scattering experiments on $AgBiSe_2$ crystals were also performed by Niedziela et al. but only the disordered rock-salt structure was observed at 640 K [58].

However, a recent study on the cubic-stabilized $AgBiSe_2$ gives us a new insight into the dynamics of cation disordering. It has been suggested that cubic $AgBiSnSe_3$ exhibits local cation ordering at room temperature, but the ordering disappears at temperatures above 550 K, which was observed by an in-situ Raman spectroscopy (Fig. 2c and e) [59]. In principle, macroscopic polarizability resulting from a periodic long-range ordering of atoms is a source of Raman peaks [60]. However, the cation intermixing at high temperatures would disrupt such periodicity, and no Raman peaks would be observed [54,61]. Given that the cation disordering is thermally activated at 550 K in cubic-stabilized $AgBiSe_2$, it is reasonable to observe disordered cubic $AgBiSe_2$ in several high-temperature measurements, since the cubic phase is only stable above the temperature at which the cation disordering occurs.

One can evaluate the electronic band structure of cation disordered $AgBiSe_2$ by constructing a supercell called “special quasirandom structure” (SQS), which mimics a perfectly random structure, as shown in Fig. 2d [62]. It is interesting to note that the disordered cubic $AgBiSe_2$ has no band gap and shows a typical band structure of metals. This is consistent with the calculation results of Hoang et al. where cation ordering is important for having an electronic band gap [55]. Indeed, the calculated electronic band structure of cubic $AgBiSe_2$ with AF-II cation ordering is significantly different from that of the disordered $AgBiSe_2$, and the band gap is estimated to be 0.065 eV (Fig. 2g) [50]. Therefore, if one observes a semiconducting behavior in cubic $AgBiSe_2$, it could be a sign that the cation ordering is present in the sample.

Significant efforts have been made to experimentally demonstrate the existence of cation ordering in ABX_2 compounds. The direct observation of cation ordering and its relationship to the transport properties was reported by Ma et al. using $AgSbTe_2$ crystals in 2013 [49]. Since the formation energy of AF-II and AF-IIb is almost energetically degenerate (only 4 meV/f. u. difference) [55], two ordering configurations exist simultaneously. This leads to a doubling of the unit cell, resulting in additional diffraction spots in the disordered lattice (Fig. 2f) [63]. Using a two-beam dark-field imaging technique, Ma et al. estimated the correlation length of the observed superstructure, which is turned out to be approximately 3 nm [49]. Similarly, high-angle annular dark-field–scanning TEM (HAADF–-STEM) imaging on $AgBiSnSe_3$ also shows a similar periodic variation of the intensity profile with a period of 2.5 nm, suggesting that the cation ordering is common in ABX_2 compounds (Fig. 2e) [64].

Table 1
Crystallographic information and physical properties of $AgBiSe_2$ at room temperature.

Empirical formula	$AgBiSe_2$
Formula weight	474.7686 g mol^{-1}
Crystal system	Trigonal
Lattice parameter (a)	4.18 Å
Lattice parameter (c)	19.67 Å
Unit cell volume	297.6287 $Å^3$
Theoretical density	7.94 g cm^{-3}
Band gap	0.6 eV
Electrical conductivity	1 S cm^{-1}
Seebeck coefficient	−276 μV K^{-1}
Thermal conductivity	0.44 W m^{-1} K^{-1}

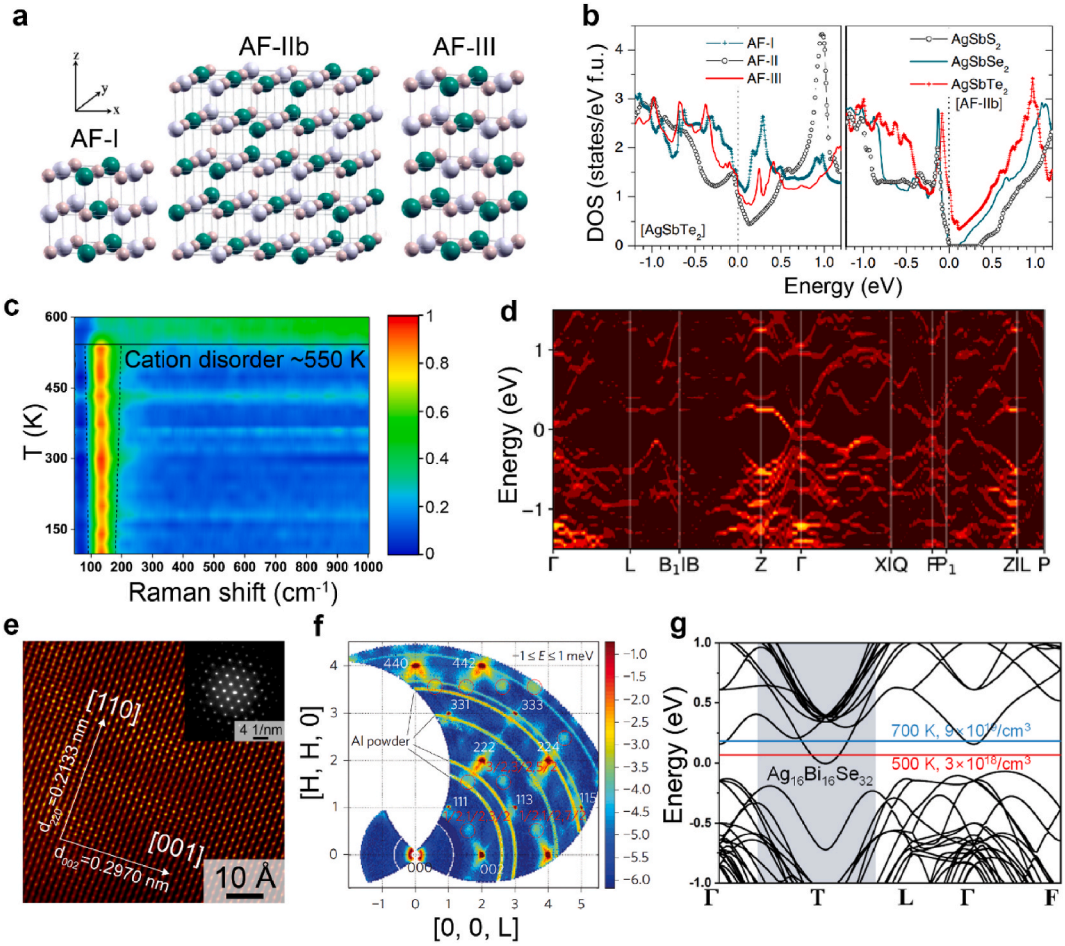

Fig. 2. Cation ordering and electronic properties. (a, b) Possible ordered structures of $AgSbTe_2$ and the electronic density-of-states of corresponding structures. Reproduced with permission from Ref. [55]. Copyright 2007, American Physical Society. (c) Temperature-dependent Raman intensity plot and (e) high-angle annular dark-field-scanning transmission electron microscopy image of $AgBiSnSe_3$. (d) Electronic band structure of $AgBiSe_2$ special quasirandom structure. Reproduced with permission from Ref. [59]. Copyright 2022, Wiley-VCH. (f) Elastic neutron scattering pattern indexed to the rock-salt structure. Red circles indicate superstructure spots. Reproduced with permission from Ref. [49]. Copyright 2013, Springer Nature. (g) Electronic band structure of $AgBiSe_2$ with the AF-II structure. Reproduced with permission from Ref. [50]. Copyright 2021, Royal Society of Chemistry.

2.3. *Thermoelectric properties of undoped $AgBiSe_2$*

Pan et al. first reported the temperature-dependent TE properties of pure, Nb-, and Pb-doped $AgBiSe_2$ in 2013 [65]. The pure $AgBiSe_2$ exhibits a negative Seebeck coefficient for temperatures up to 773 K, implying that the electron is the majority carrier in undoped $AgBiSe_2$ (Fig. 3a). The magnitude of the Seebeck coefficient increases with temperature while the electrical conductivity decreases (Fig. 3b). This is a typical behavior of a degenerate semiconductor with high carrier concentration. The Seebeck coefficient and electrical conductivity of pure $AgBiSe_2$ are approximately $-150\ \mu V\ K^{-1}$ and $67\ S\ cm^{-1}$, respectively. Two humps are observed in the electrical properties at 480 K and 580 K (black arrows in Fig. 3a–b), resulting from the phase transitions discussed in Section 2.1. The carrier concentration of undoped $AgBiSe_2$ reported by Pan et al. is approximately $1.8 \times 10^{19}\ cm^{-3}$ and the corresponding Hall mobility is approximately $30\ cm^2\ V^{-1}\ s^{-1}$. However, Zou et al. reported the Seebeck coefficient and electrical conductivity of $AgBiSe_2$ to be $-290\ \mu V\ K^{-1}$ and $55\ S\ cm^{-1}$, respectively [66]. The carrier concentration measured by Zou et al. was approximately $3 \times 10^{18}\ cm^{-3}$, which is relatively lower than that measured by Pan et al.

The temperature-dependent thermal conductivity of $AgBiSe_2$ is shown in Fig. 3c. The pure $AgBiSe_2$ shows a low thermal conductivity value of $0.65\ W\ m^{-1}\ K^{-1}$ at 300 K. The temperature dependence of the thermal conductivity does not follow the conventional T^{-1} dependence. Morelli et al. attribute the possible reason for the unconventional behavior of the thermal properties to the high Grüneisen parameter of $AgBiSe_2$ [47]. Typically, the lattice thermal conductivity, where only the Umklapp process dominates the phonon scattering is given by

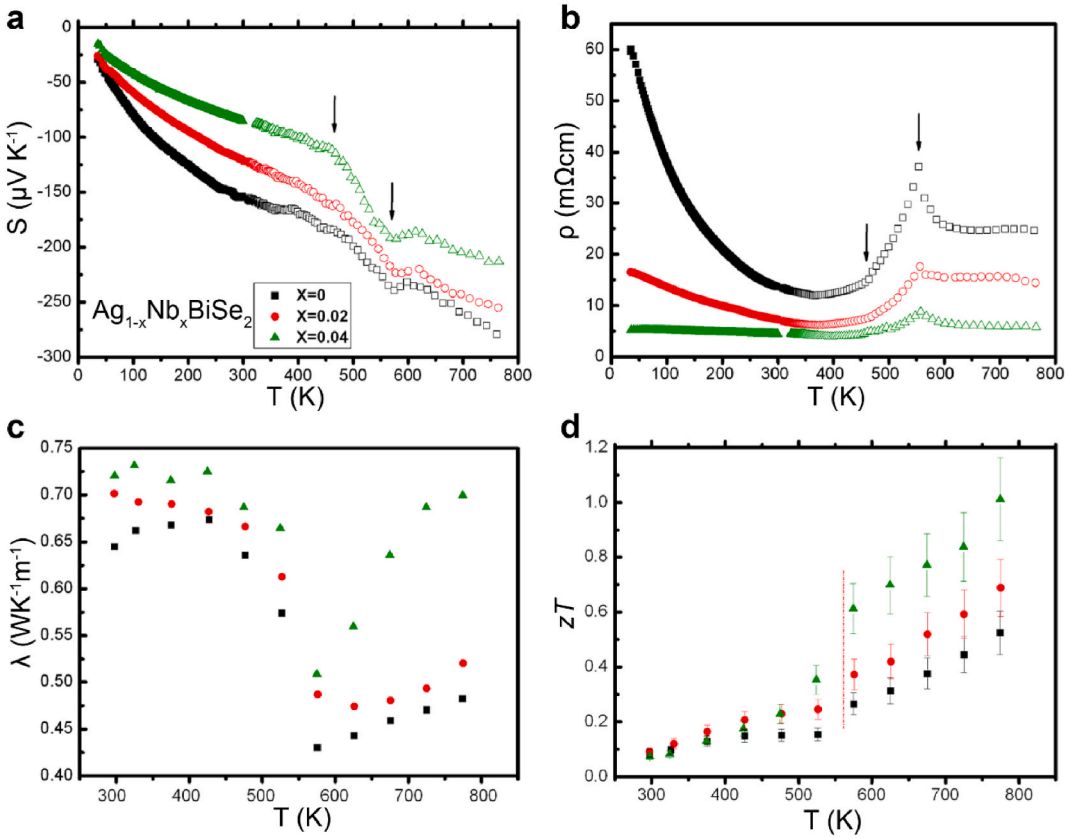

Fig. 3. Thermoelectric properties of pure and Nb-doped $AgBiSe_2$. Temperature-dependent (a) Seebeck coefficient, (b) electrical resistivity, (c) total thermal conductivity, and (d) zT values. Reproduced with permission from Ref. [65]. Copyright 2013, American Chemical Society.

$$\kappa_L = A\frac{\overline{M}\theta^3\delta}{\gamma^2 n^{2/3} T} \quad \text{(Equation 1)}$$

where γ is the Grüneisen parameter, n is the number of atoms in the primitive unit cell, δ^3 is the volume per atom, θ is the Debye temperature, $\overline{M}$ is the average mass of the atoms in the crystal, and A is a constant (approximately 3.1×10^{-6}) [67]. The high Grüneisen parameter implies that the anharmonic scattering of phonons occurs frequently, leading to a short phonon mean free path. However, under the assumption of the phonon gas model, the mean free path of phonons cannot be shorter than the interatomic distance [68]. Therefore, the unusual thermal transport properties of $AgBiSe_2$ can be understood by the result of the high Grüneisen parameter and the extremely short phonon mean free path. The undoped $AgBiSe_2$ shows a relatively high zT value of 0.45 at 773 K, and the Nb doping even increases it to approximately 1.0 at 773 K (Fig. 3d). This enhancement is the result of Fermi level tuning, which will be discussed in the following section.

2.4. *Doping strategies for controlling electrical properties*

$AgBiSe_2$ has a relatively low electrical conductivity (~1 S cm^{-1}) compared to other known TE materials such as $AgSbTe_2$ (~160 S cm^{-1}) [38,69], $Sb_2Si_2Te_6$ (~550 S cm^{-1}) [70,71], and SnTe (~8000 S cm^{-1}) [72,73]. Therefore, improving the electrical conductivity by tuning the Fermi level would be one of the most feasible ways to increase the zT values of $AgBiSe_2$. Since $AgBiSe_2$ is intrinsically an n-type semiconductor, most research has been focused on incorporating donor defects into $AgBiSe_2$. For example, Guin et al. substituted halogen elements (e.g., Cl, Br, and I) in Se sites to increase the electron concentration [74]. According to a simple valence electron counting rule, for a given halogen element X, substituting Se sites into X donates one electron per X atom by the following defect equation: $Se_{Se}^{x} \rightarrow X_{Se}^{\bullet} + e'$. The measured electron concentration of undoped, 2 % Cl-doped, 2 % Br-doped, and 2 % I-doped $AgBiSe_2$ was 5.85×10^{18} cm^{-3}, 3.72×10^{19} cm^{-3}, 4.63×10^{19} cm^{-3}, and 3.98×10^{19} cm^{-3}, respectively. It can be noted that the doping efficiency of Br is the highest among the halogen elements, presumably due to similarities in ionic radius (198 pm and 196 pm for Se^{2-} and Br^{-}, respectively [75]) and electronegativity (3.37 and 3.45 for Se and Br, respectively [76]) as expected by the Hume-Rothery rules. Interestingly, the carrier concentration remained similar (~4.65×10^{19} cm^{-3}) while the doping concentration was doubled (i.e., 4 % halogen doped), implying that the maximum solubility limit might be reached already at 2 % doping concentration. Fig. 4a-c shows the effect of halogen doping in $AgBiSe_2$. The electrical conductivity increases as a result of the increased

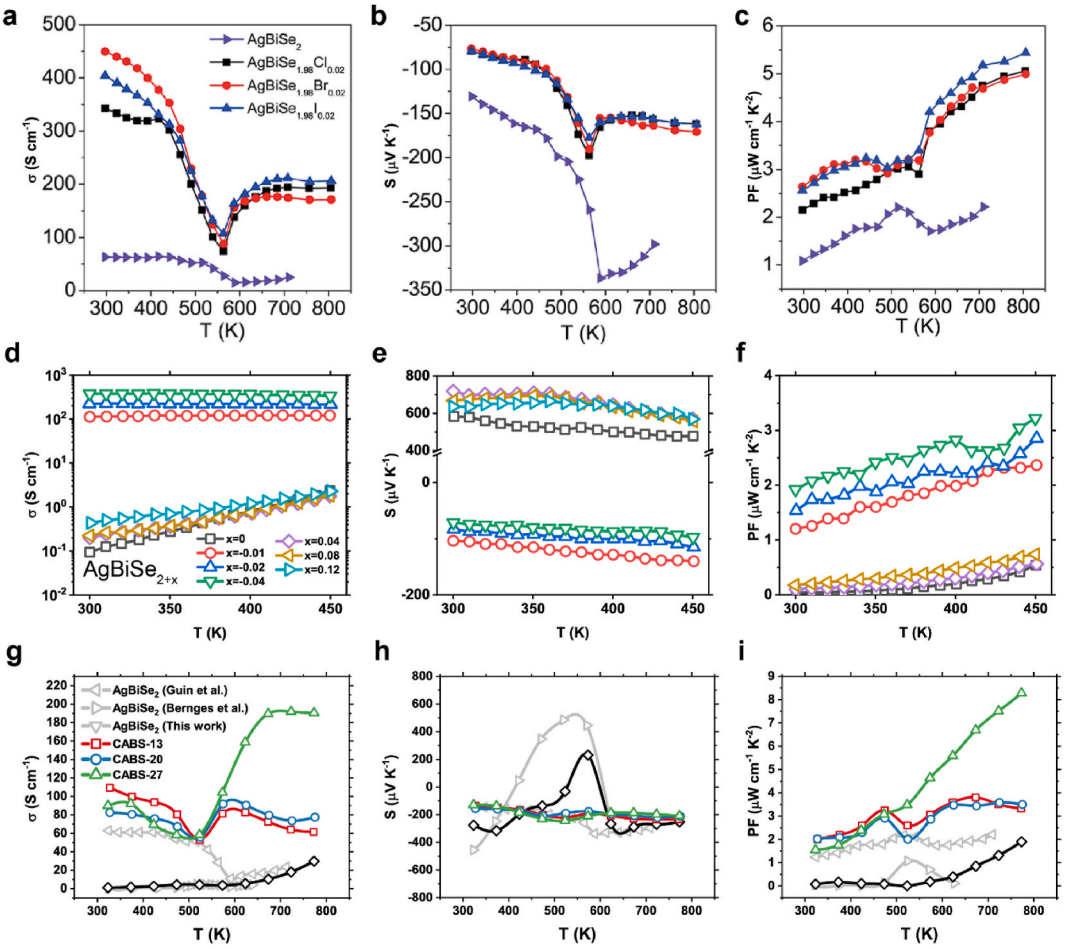

Fig. 4. Modulation of electrical properties of $AgBiSe_2$. Temperature-dependent electrical conductivity (a, d, g), Seebeck coefficient (b, e, h), and power factor (c, f, i) upon doping. (a–c) Electrical properties of halogen doped $AgBiSe_2$. Reproduced with permission from Ref. [74]. Copyright 2015, Royal Society of Chemistry. (d–f) Electrical properties of $AgBiSe_2$ by adding excess Se. Reproduced with permission from Ref. [80]. Copyright 2020, American Chemical Society. (g–h) Electrical properties of Cu-doped $AgBiSe_2$. Reproduced with permission from Ref. [50]. Copyright 2021, Royal Society of Chemistry.

carrier concentration, and the Seebeck coefficient decreases according to the inverse relationship between the carrier concentration and the Seebeck coefficient [7]. One can also increase the electron concentration of $AgBiSe_2$ by substituting cations to form donor defects. For example, Pan et al. incorporated Nb atoms into Ag sites to increase the electron concentration, resulting in an improved electrical conductivity of ~200 S cm^{-1} at room temperature [65]. The maximum carrier concentration achievable with Nb doping was approximately 8.2×10^{19} cm^{-3}, which is slightly higher than that for Br-doped $AgBiSe_2$. In is also known to be an effective donor when replacing Ag sites [77–79].

The electrical properties of $AgBiSe_2$ can also be tuned by controlling the stoichiometry of the starting materials to adjust the chemical potential of the constituent elements. Li et al. demonstrated that both electrical conductivity and carrier polarity can be controlled by the amount of elemental Se before melting (Fig. 4d-f) [80]. They found that the Seebeck coefficient becomes positive in the presence of excess Se, while the Seebeck coefficient becomes negative when the Se content is deliberately reduced. Understanding the mechanism to achieve p-type conduction in $AgBiSe_2$ is of high importance because $AgBiSe_2$ is expected to show significantly improved TE properties when holes dominate charge conduction [81]. However, achieving p-type conduction in $AgBiSe_2$ has been challenging due to the extremely low p-type dopability of $AgBiSe_2$. For example, $AgSbSe_2$ is known to be an intrinsically p-type semiconductor [82], but substitution of Bi sites for Sb in $AgBiSe_2$ does not significantly increase the hole concentration [83] or even shows n-type properties despite being heavily doped with Sb [84]. Pb doping at Bi sites is known to reproducibly convert $AgBiSe_2$ from n-to p-type, but it is impractical to be used as a TE material because the low p-type dopability of $AgBiSe_2$ results in an extremely high resistivity of Pb-doped $AgBiSe_2$ [65]. Therefore, the finding that Se-related defects determine the carrier polarity is helpful in understanding the defect environment of $AgBiSe_2$. In addition, Li et al. found that the introduction of Ag vacancies does not increase the hole concentration, although Ag vacancies were expected to be the defect responsible for the p-type conductivity in $AgBiSe_2$ by the experiments and computational results of Xiao et al. [54].

Finally, band engineering of $AgBiSe_2$ can be achieved by incorporating Cu to the Ag sites, as shown in Fig. 4g-i. Jang et al. reported the band nestification of conduction bands to improve the power factor (PF) of n-type $AgBiSe_2$ [50]. The band nestification is a type of band convergence, where multiple electronic bands are in an energetically degenerate state to increase the valley degeneracy [12]. However, unlike band convergence, which shows multiple degenerate bands at different k-space locations, band nestification refers to an increase in valley degeneracy by converging two or more electronic bands at the same k-space location [85]. In both cases, the multiple bands should result in improved TE properties owing to the increased DOS effective mass but preserved carrier mobility; however, the band nestification may be beneficial in the material system where intervalley scattering is significantly detrimental to the overall TE properties [86]. Experimentally, Jang et al. observed a significant increase in the DOS effective mass after the cubic phase transition in Cu-doped $AgBiSe_2$ sample, while it remained similar in the trigonal structure. Using the DFT calculations, it was found that the incorporation of Cu atoms into $L1_1$-type $AgBiSe_2$ increases the valley degeneracy at the T-point, and hypothetical cubic compound $CuBiSe_2$ had the highest valley degeneracy at the T-point among all $AgBiSe_2$–$CuBiSe_2$ alloys. The increased valley degeneracy due to Cu doping was also confirmed in the $D4$ structure, but not in the trigonal structure; therefore, improved electrical properties should be observed only after the cubic phase transition in Cu-doped $AgBiSe_2$. Indeed, the PF values are significantly higher in CABS-27 (the sample with the highest Cu concentration) after 523 K, which supports the idea that the band nestification effect is present in the cubic phase. Unlike the carrier concentration tuning, band convergence or band nestification does not necessarily follow a conventional trade-off relationship between the Seebeck coefficient and electrical conductivity, which results from the inversely proportional relationship between the inertial effective mass and carrier mobility [87]. Therefore, Cu-doped $AgBiSe_2$ shows high PF values at 773 K owing to the synergistic enhancement of the DOS effective mass and the electrical conductivity (see Table 2).

2.5. Phonon engineering of $AgBiSe_2$ with doping and alloying

As mentioned above, $AgBiSe_2$ has the high Grüneisen parameter, which leads to an extremely low lattice thermal conductivity and unconventional temperature dependence. However, in the trigonal structure, there are some reports that have analyzed the doping/alloying effects of isovalent impurities (e.g., Te doping on Se sites or Sb doping on Bi sites). Goto et al. reported the effect of Te alloying in $AgBiSe_2$ and found that the reduction of the lattice thermal conductivity at room temperature is mainly dominated by the both the mass and strain contrast arising from the Te alloying (Fig. 5a–d) [88]. The undoped $AgBiSe_2$ showed the lattice thermal conductivity value of approximately 0.6 W m^{-1} K^{-1} at 300 K, but it showed a gradual decrease with increasing Te concentration. The Debye-Callaway modelling of the theoretical lattice thermal conductivity is helpful to understand the reduction of the lattice thermal conductivity with doping. The total scattering rate (inverse of the relaxation time) of the phonons is given by the sum of the scattering rates for each process by Matthiessen's rule. For example, considering Umklapp process, normal process, and point defects scattering, the total scattering rate is given by:

$$\tau_{tot}^{-1} = \tau_U^{-1} + \tau_N^{-1} + \tau_{PD}^{-1} \quad \text{(Equation 2)}$$

where U, N, and PD denote Umklapp, normal, and point defects scattering, respectively. Assuming that the scattering rate of Umklapp and normal processes remains similar upon doping, the point defects scattering mechanism should be responsible for the reduced lattice thermal conductivity. The scattering rate by point defects is given by:

Table 2
Summary of thermoelectric properties of n-type $AgBiSe_2$-based materials.

Composition	Preparation methods[a]	Seebeck coefficient (μV/K)	Electrical conductivity (S/cm)	Total thermal conductivity (W/m·K)	zT	Ref.
$\mathbf{Ag_{0.96}Nb_{0.04}BiSe_2}$	MS + SPS	−215	200	0.7	1 @ 773K	[65]
$\mathbf{AgBiSe_{1.2}Te_{0.8}}$	SSR + HP	−145	185	0.6	0.6 @ 773 K	[88]
$\mathbf{Ag_{0.985}In_{0.015}BiSe_2}$	MS + SPS	−185	125	0.5	0.7 @ 773 K	[78]
$\mathbf{AgPbBiSe_{2.98}Cl_{0.02}}$	MS	−155	180	0.5	0.9 @ 810 K	[74]
$\mathbf{Ag_{0.97}Ge_{0.03}Bi_{0.97}Se_{1.97}}$	BR	−105	330	0.25	1.1 @ 748 K	[90]
$\mathbf{Ag_{0.992}BiIn_{0.008}Se_{1.6}S_{0.4}}$	MS + BM + SPS	−220	80	0.33	0.9 @ 773 K	[79]
$\mathbf{Cu_{0.27}Ag_{0.73}BiSe_2}$	MS + SPS	−210	190	0.56	1.1 @ 773 K	[50]
$\mathbf{Ag_{0.93}BiSe_2}$	MS + CP + A	−160	60	0.6	0.32 @ 600 K	[89]
$\mathbf{(Ag_{0.995}In_{0.005}BiSe_{1.99}S_{0.01})_{0.95}(Ag_2Se)_{0.05}}$	MS + BM + SPS	−150	180	0.4	0.94 @ 773 K	[77]

[a] MS: melting and solidification; SSR: solid state reaction; HP: hot pressing; BR: Bridgman method; BM: ball milling; CP: cold pressing; A: annealing. The thermoelectric properties summarized in the table are the values at which the maximum zT value is measured.

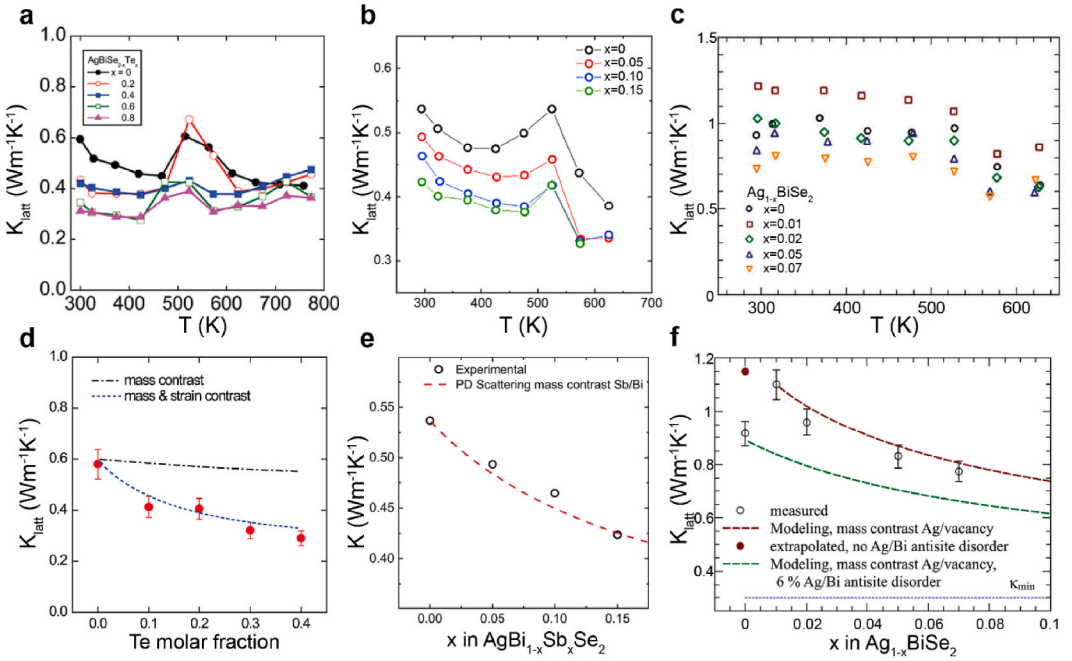

Fig. 5. Reducing thermal conductivity of $AgBiSe_2$ with doping and alloying. (a) Temperature-dependent lattice thermal conductivity and (d) Debye-Callaway modelling of the lattice thermal conductivity of $AgBiSe_{2-x}Te_x$. Reproduced with permission from Ref. [88]. Copyright 2018, Royal Society of Chemistry. (b) Temperature-dependent lattice thermal conductivity and (d) Debye-Callaway modelling of the lattice thermal conductivity of $AgBi_{1-x}Sb_xSe_2$. Reproduced with permission from Ref. [83]. Copyright 2019, American Chemical Society. (c) Temperature-dependent lattice thermal conductivity and (f) Debye-Callaway modelling of the lattice thermal conductivity of $Ag_{1-x}BiSe_2$. Reproduced with permission from Ref. [89]. Copyright 2017, Royal Society of Chemistry.

$$\tau_{PD}^{-1} = \frac{\overline{V}\omega^4}{4\pi v^3}\Gamma \qquad \text{(Equation 3)}$$

where $\overline{V}$, ω, v, and Γ is the average atomic volume, phonon frequency, average sound velocity, and point defects scattering parameter. Here, the origin of Γ comprises of two components: mass and strain contrast between host and the guest atoms. Γ is mathematically expressed by:

$$\Gamma = x(1-x)\left[\left(\frac{\Delta M_{A,B}}{M_{A,B}}\right)^2 + \varepsilon\left(\frac{\Delta r_{A,B}}{r_{A,B}}\right)^2\right] \qquad \text{(Equation 4)}$$

where the first term accounts for the mass contrast between A and B atoms, while the second term reflects the strain contrast resulting from the difference of the atomic radius between A and B atoms. The measured lattice thermal conductivity in Fig. 5d is well fitted by the theoretically expected lattice thermal conductivity with the point defects scattering model when two contributions are considered simultaneously. However, the theoretical lattice thermal conductivity is significantly overestimated when the strain contrast is neglected and only the mass contrast is included in the calculation. The difference in molar mass between Se (78.96 g mol^{-1}) and Te (127.6 g mol^{-1}) is approximately 47.1 %, while the difference in ionic radius between Se^{2-} (198 pm) and Te^{2-} (221 pm) is only 11.0 %. This means that the lattice strain has a significant effect on the suppression of phonon transport in a material. However, the thermal conductivity data of $AgBi_{1-x}Sb_xSe_2$ alloys reported by Bernges et al. are puzzling to understand the thermal behavior of $AgBiSe_2$ (Fig. 5b–e) [83]. Here, the isovalent counterpart, Sb, was used as a dopant to substitute Bi sites. The percentage difference in atomic mass between Bi (208.9804u) and Sb (121.76u) is 52.7 %, while that arising from the ionic radius difference between Bi (103 pm) and Sb (76 pm) is 30.2 %. In this case, the contribution of strain contrast was much higher compared to the case of $AgBiSe_{2-x}Te_x$ alloys, but Bernges et al. successfully fitted the theoretical lattice thermal conductivity of $AgBi_{1-x}Sb_xSe_2$ alloys without including the effect of strain contrast. Therefore, a more sophisticated study on the effect of dopants on the thermal behavior of $AgBiSe_2$ should be performed.

The reason for the complicated thermal transport properties of $AgBiSe_2$ may be related to the formation of antisite defects in $AgBiSe_2$ [89,90]. Böcher et al. investigated the effect of introducing Ag vacancies on the TE properties of $AgBiSe_2$ by synthesizing non-stoichiometric $Ag_{1-x}BiSe_2$ samples. Interestingly, the lattice thermal conductivity of stoichiometric $AgBiSe_2$ (approximately 0.91 W m^{-1} K^{-1}) is lower than that of Ag vacancy-doped $Ag_{0.99}BiSe_2$ (approximately 1.1 W m^{-1} K^{-1}), which is contraty to the result expected from the point defects scattering model (Fig. 5c). However, X-ray refinement study on vacancy-introduced $AgBiSe_2$ samples revealed that the existence of Bi-on-Ag (Bi_{Ag}) antisite defects, and the concentration of Bi_{Ag} decreases with increasing Ag vacancy concentration. They claimed that the faster movement of Bi^{3+} ions is possible with increasing the vacancy concentration, because

vacancy sites act as a pathway for the diffusion process. This observation may explain why the wide range of the lattice thermal conductivity values is reported for the undoped $AgBiSe_2$. The concentration of vacancies and the resulting antisite defects can vary depending on the synthesis conditions and the purity of the starting materials. In addition, the high volatility of Se may lead to an unexpected stoichiometry that is different from the nominal composition. Therefore, an unusual increase in the lattice thermal conductivity with vacancy doping could be explained by the reduced Bi_{Ag} concentration, as shown in Fig. 5f.

2.6. *Entropic stabilization of cubic $AgBiSe_2$ and its properties*

Although the temperature-dependent polymorphism of $AgBiSe_2$ is scientifically intriguing and deserves to be studied in depth, the huge volume change during the phase transition and significant formation of Bi_2Se_3 secondary phases due to the low phase stability of trigonal $AgBiSe_2$ have been serious problems for the practical application of $AgBiSe_2$ for a power generation purpose [66]. Therefore, a

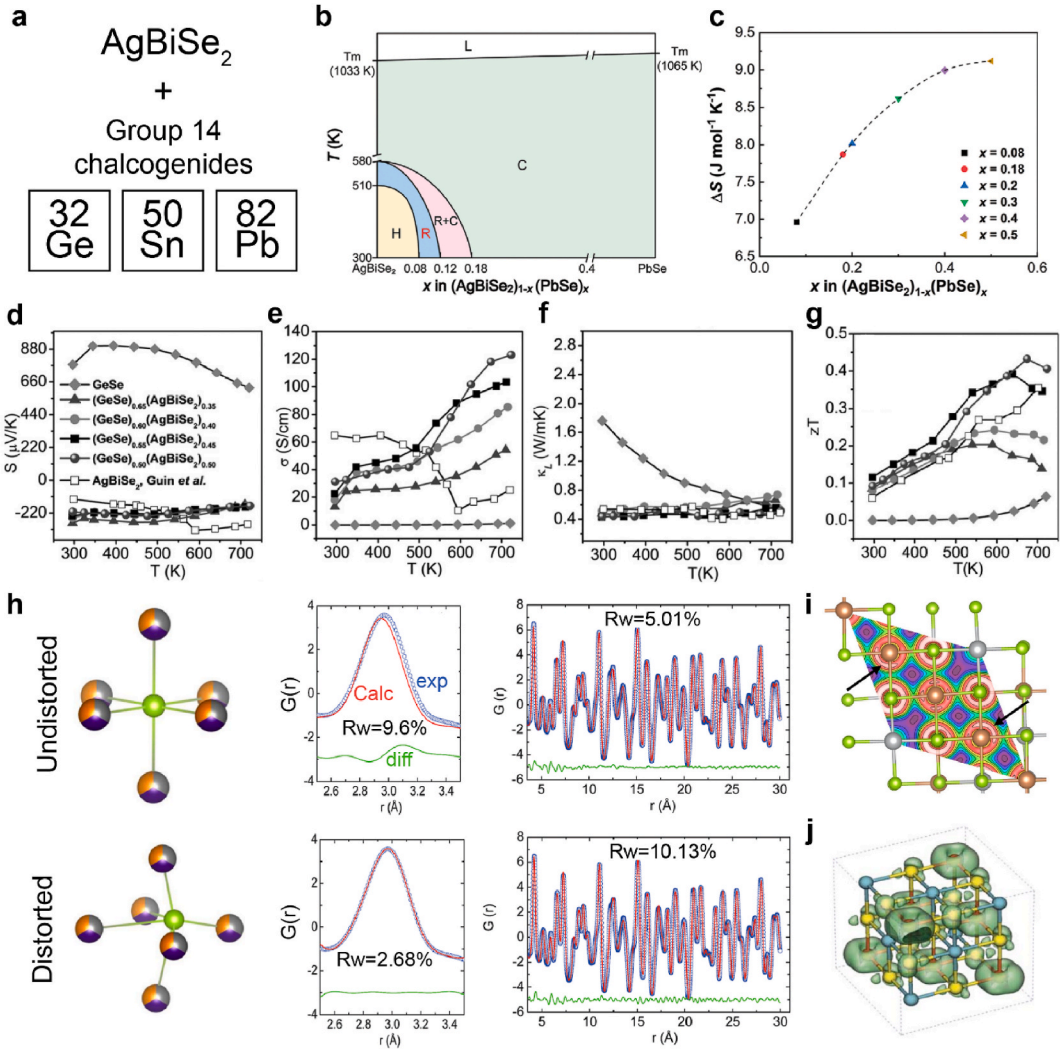

Fig. 6. Effect of cubic phase stabilization on $AgBiSe_2$. (a) Typical elements alloyed with $AgBiSe_2$ to stabilize the cubic phase. (b) Phase diagram of $(AgBiSe_2)_{1-x}(PbSe)_x$ alloys. H, R, and C denotes the hexagonal (trigonal), rhombohedral, and cubic phases, respectively. (c) Calculated mixing entropy with the alloying fraction by ideal mixing model. Reproduced with permission from Ref. [105]. Copyright 2020, Wiley-VCH. (d–g) Temperature-dependent (d) Seebeck coefficient, (e) electrical conductivity, (f) lattice thermal conductivity, and (g) zT values of $AgBiSe_2$–GeSe alloys. Reproduced with permission from Ref. [99]. Copyright 2018, Wiley-VCH. (h) Schematic of the cation off-centering in the presence of lone-pair electrons. Reproduced with permission from Ref. [115]. Copyright 2021, American Chemical Society. Corresponding PDF profile with refinement results with and without cation off-centering model is given together. Reproduced with permission from Ref. [104]. Copyright 2019, Royal Society of Chemistry. (i) Calculated electron localization function (ELF) map of $AgSbSe_2$. The asymmetric distribution of lone-pair electrons near the Sb atoms (orange) is indicated by black arrows. Reproduced with permission from Ref. [48]. Copyright 2022, Wiley-VCH. (j) Calculated electronic polarization of $L1_1$ $NaSbSe_2$ by an external electric field. The dipole moment is the strongest in Sb atoms. Reproduced with permission from Ref. [111] Copyright 2008, Royal Society of Chemistry.

concept of entropy engineering has been recently introduced to stabilize cubic $AgBiSe_2$ at room temperature by means of suppressing an abrupt change in physical properties for a reliable operation at high temperatures. In general, the cubic phase transition occurs when the Gibbs free energy of the cubic phase is lower than that of the trigonal (or rhombohedral) phase. The difference in the Gibbs free energy between the trigonal and cubic phases can be expressed as follows:

$$\Delta G_{R-C} = \Delta H_{R-C} - T\Delta S_{R-C} \quad \text{(Equation 5)}$$

where ΔG_{R-C}, ΔH_{R-C}, and ΔS_{R-C} is the difference of Gibbs free energy, enthalpy, and entropy of the rhombohedral-to-cubic phase transition. ΔG_{R-C} of pure $AgBiSe_2$ is expected to be zero at approximately 573 K, since DSC analyses indicate that the phase transition occurs at that temperature [64,91]. Assuming that the phase transition enthalpy (ΔH_{R-C}) remains constant, increasing the transition entropy (ΔS_{R-C}) would be an effective way to lower the temperature that is required to compensate ΔH_{R-C}. One can note that ΔS_{R-C} can be increased by adding multiple chemical components in a material to include a contribution from mixing entropy, ΔS_{mix}. Thermodynamically, the ideal ΔS_{mix} is approximated as follows:

$$\Delta S_{mix} = -R\sum_{i=1}^{N} x_i \, ln \, x_i \quad \text{(Equation 6)}$$

where x_i is the atomic fraction of element i, k_B is the Boltzmann constant, and N is the number of elements [92,93]. Indeed, it has been experimentally observed that the transition temperature decreases as the number of elements increases in several material systems [50, 91,94–98].

Typically, $AgBiSe_2$ is alloyed with the group 14 elements such as Ge [99,100], Sn [64,101–103], and Pb [104–107] to form solid solutions and stabilize the cubic phase (Fig. 6a). For example, Huaxing et al. investigated the effect of PbSe alloying on the transition temperature of $AgBiSe_2$, as shown in Fig. 6b. They found that the cubic phase coexisted with the rhombohedral phase in $(AgBiSe_2)_{0.88}(PbSe)_{0.12}$, while only the cubic phase was stable when the PbSe fraction was above 0.18. The calculated mixing entropy of $(AgBiSe_2)_{1-x}(PbSe)_x$ alloys is shown in Fig. 6c. The mixing entropy increases with increasing x up to 0.5, and then decreases. Interestingly, Roychowdhury et al. [99] and Jang et al. [64] reported the stable cubic region to be above 30 % of the alloying end-member in $AgBiSe_2$–GeSe and $AgBiSe_2$–SnSe solid solutions, respectively. Since the mixing entropy does not account for the difference of chemical species in the calculation, it is reasonable to assume that contributions other than increased mixing entropy affect the stabilization of cubic $AgBiSe_2$. Similarly, Sb alloying to Bi sites can increase ΔS_{mix} to stabilize the cuibic phase $AgBiSe_2$ [108].

The thermoelectric properties of $AgBiSe_2$–GeSe alloys are shown in Fig. 6d–g. GeSe is intrinsically a p-type semiconductor with a positive Seebeck coefficient for 300–700 K. The reason for this p-type conduction is mainly due to the formation of Ge vacancies, which are thermodynamically preferred in both Ge-rich and Se-rich conditions [109], although the hole concentration of undoped GeSe is relatively low ($\sim 10^{16}$ cm^{-3}) [110]. However, 35 % alloying of $AgBiSe_2$ completely converts GeSe into an n-type semiconductor, showing a strong electron-donating property of $AgBiSe_2$ when used as an alloying end-member. It should be noted that the defect chemistry of GeSe, $AgBiSe_2$, and their alloys may be significantly different due to the change in crystal structure upon alloying. The reported electrical properties of $AgBiSe_2$–GeSe alloys are those of cubic-phase-stabilized compositions (alloying fraction over 30 %). The electrical conductivity of $AgBiSe_2$-alloyed GeSe is significantly enhanced due to the increased carrier concentration ($\sim 3.29 \times 10^{18}$ cm^{-3}) compared to that of undoped GeSe. The temperature dependence of Seebeck coefficient and electrical conductivity of $AgBiSe_2$–GeSe alloys show non-degenerate characteristics. Temperature-dependent lattice thermal conductivity in Fig. 6f is clearly showing a unique thermal behavior of cubic phase $AgBiSe_2$. GeSe shows a typical T^{-1} dependence of the lattice thermal conductivity, revealing its Umklapp-process-dominant phonon transport. However, other $AgBiSe_2$–GeSe alloys do not show a significant decrease in the lattice thermal conductivity upon alloying, which is in directly contradiction to the results expected by the Debye-Callaway model. As discussed in Section 2.2, the spontaneous nanostructure of cubic I-V-VI_2 semiconductors may limit the phonon mean free path down to the interatomic distance, resulting in the minimal lattice thermal conductivity of a material and moderately high zT values (Fig. 6g).

Another possible explanation is the presence of lone-pair electrons which contribute significantly to the high lattice anharmonicity. Nielsen et al. studied the thermal behavior of cubic I-V-VI_2 semiconductors and found that the lone-pair-containing materials share two common characteristics: the extremely low lattice thermal conductivity and the unchanged lattice thermal conductivity with alloying or temperature [111]. The lone-pair electrons exist in the s-orbital of the group V element in I-V-VI_2 semiconductors, and exhibit high polarizability in response to the external electric field (Fig. 6j). Therefore, the perturbation of the electron density by the vibration of the atoms (which acts similarly to the external electric field) will induce a huge dipole moment of the lone-pair electrons, contributing to the increased electrostatic interactions between atoms and high lattice anharmonicity. Dutta et al. demonstrated the existence of lone-pair electrons in $AgSbSe_2$ by electron localization function (ELF) via DFT calculations. ELF is a measure of electron localization in the crystal lattice, where ELF = 1 represents the perfect localization, ELF = 0.5 corresponds to the electron gas, and ELF = 0 represents the absence of electron localization [112]. Typically, the two-dimensional projection of ELF directly reveals an existence of lone-pair electrons by the asymmetric distribution of high ELF regions near a given element, as in the case of lone-pair electrons in $AgSbSe_2$ (Fig. 6i). Alternatively, it can be visualized by polarization current density under an applied external field, as demonstrated by Nielsen et al. in $L1_1$ $NaSbSe_2$ (Fig. 6j) [111].

Interestingly, lone-pair electrons are often stereochemically active, resulting in an off-centering of cations in compounds with a rock-salt structure [48,113–115]. This can be measured experimentally using a sophisticated powder X-ray diffraction (XRD) technique called pair distribution function (PDF) analysis. The conventional powder XRD technique uses the Bragg diffraction where long-range periodicity is strongly reflected in the measured spectra. However, it is relatively difficult to characterize materials that are

nanocrystalline, highly disordered, or not fully periodic using conventional powder XRD [116]. PDF uses both the Bragg diffraction and diffuse scattering to obtain the short-range order and atomic-scale features by the Fourier transform of diffraction intensities. The atomic PDF, G(r), is given by:

$$G(r) = \frac{2}{\pi} \int_{Q=0}^{Q_{max}} Q[S(Q) - 1]\sin(Qr)dQ \quad \text{(Equation 7)}$$

where Q is the magnitude of the scattering vector, $S(Q)$ is the normalized scattering intensity, r is the radial distance, and Q_{max} is the cutoff of the obtained signal [117]. Using this technique, Dutta et al. found that the undistorted rock-salt structure cannot adequately fit the short-range-order region (2.5 Å $< r <$ 3.5 Å), although it gave a satisfactory fit for long-range-order region ($r >$ 3.5 Å) in cubic $AgPbBiSe_3$ (Fig. 6h) [104]. However, the fit was improved using a cation off-centered structure in the short-range-order region. This observation confirms the cation off-centering in cubic $AgBiSe_2$-based compounds and suggests that stereochemically active lone-pair electrons may be present in these materials.

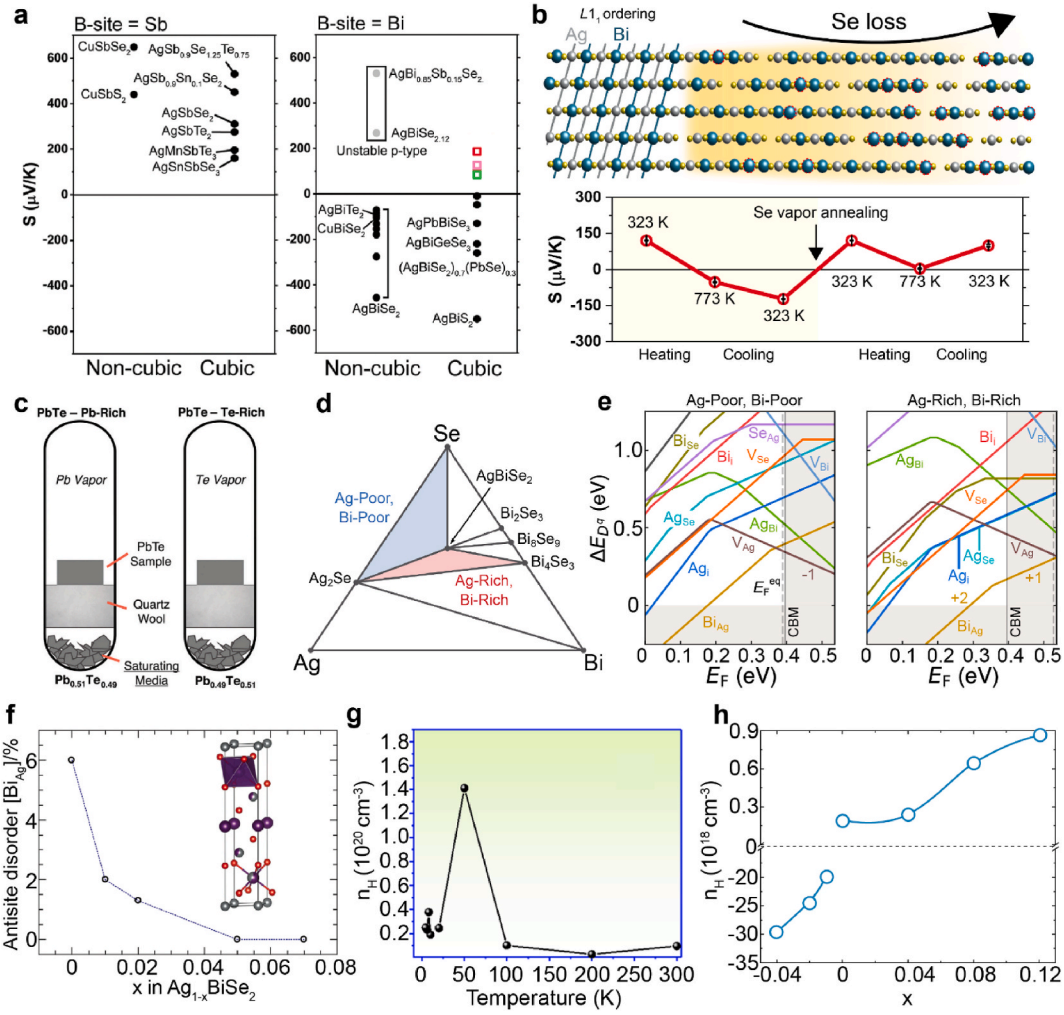

Fig. 7. Control of point defects for achieving bipolar dopability in $AgBiSe_2$. (a) B-site cation dependent Seebeck coefficient of ABX_2 compounds. (b) Effect of Se vapor annealing on the Seebeck coefficient of cubic $(AgBiSe_2)_{0.6}(SnSe)_{0.4}$. Reproduced with permission from Ref. [64]. Copyright 2022, Wiley-VCH. (c) Schematic diagram showing a typical configuration of saturation annealing. Reproduced with permission from Ref. [118]. Copyright 2019, Royal Society of Chemistry. (d) Ternary phase diagram of $AgBiSe_2$ and two representative thermodynamic conditions for Ag-poor and Bi-poor (blue) and Ag-rich and Bi-rich (red). (e) Calculated point defect formation energy under two thermodynamic conditions from (d). Reproduced with permission from Ref. [64]. Copyright 2022, Wiley-VCH. (f) The concentration of Bi_{Ag} with Ag vacancy doping in trigonal $AgBiSe_2$. Reproduced with permission from Ref. [89]. Copyright 2017, Royal Society of Chemistry. (g) Hall carrier concentration of trigonal-phase single crystal $AgBiSe_2$ showing hole-dominated conduction property. Reproduced with permission from Ref. [119]. Copyright 2022, IOP Publishing Ltd. (h) Change of conduction type in $AgBiSe_{2+x}$. Reproduced with permission from Ref. [80]. Copyright 2020, American Chemical Society.

2.7. Defect-controlled conduction type and bipolar dopability of $AgBiSe_2$

TE devices mainly consist of alternating n- and p-type legs; therefore, the bipolar dopability of TE materials is critical for the realization of TE modules. However, most $AgBiSe_2$-based materials are known to exhibit n-type properties. As shown in Sections 2.3 and 2.4, most $AgBiSe_2$-based TE materials exhibit negative Seebeck coefficients, implying that electrons are majority carriers. In principle, the conduction type of an intrinsic semiconductor without any impurity should be determined by the intrinsic point defects present in the material. Because of its n-type nature, $AgBiSe_2$ was thought to have Se vacancies (V_{Se}), which would act as electron donors [80]. However, this claim is puzzled by the sign of the reported Seebeck coefficient of $AgBiS_2$, $AgBiSe_2$, and $AgBiTe_2$, where all three compounds exhibit electron-dominated charge transport (Fig. 7a). Furthermore, when the B-site cation is changed from Bi to Sb, the sign of the Seebeck coefficient becomes positive. Therefore, it is reasonable to assume that the B-site cation is determining the conductivity type in ABX_2 compounds. In other words, Bi-based compounds have more donor-like defects, while Sb-based compounds have more acceptor-like defects.

Jang et al. experimentally demonstrated a sign reversal of the Seebeck coefficient before and after Se vapor annealing in $AgBiSe_2$–SnSe alloys [64]. For example, $(AgBiSe_2)_{0.6}(SnSe)_{0.4}$ initially showed p-type conductivity at room temperature, but changed to n-type semiconductor at 773 K and did not return to p-type after cooling (Fig. 7b). This phenomenon is observed only when the sample is measured under high vacuum, and the sample retains its p-type property under He cover gas. However, when the sample was sealed with elemental Se and annealed at 773 K for 24 h, the sample recovered the p-type property. This process is called "saturation annealing," which is used to study phase boundary effects by subjecting samples to different thermodynamic conditions and measuring the change in properties [34,118]. Typically, saturation annealing is performed by annealing the sample with saturating media that has a slightly off-stoichiometric composition compared to the original sample. For example, PbTe can be prepared in either Pb-rich or Te-rich conditions by annealing PbTe samples with $Pb_{0.51}Te_{0.49}$ (for Pb-rich samples) or $Pb_{0.49}Te_{0.51}$ (for Te-rich samples) as shown in Fig. 7c [118]. Similarly, annealing $(AgBiSe_2)_{0.6}(SnSe)_{0.4}$ with elemental Se would push the thermodynamic condition of a sample toward Se-rich conditions.

To compare the phase boundary effect in $AgBiSe_2$, two representative thermodynamic conditions (Ag-poor, Bi-poor/Ag-rich, Bi-rich) can be considered to calculate the defect formation energy of cubic $AgBiSe_2$ by DFT (Fig. 7d–e). In both cases, the formation of Bi_{Ag} is the most preferred donor-like defect, while acceptor-like V_{Ag} compensates Bi_{Ag}. However, compared to the Ag-rich and Bi-rich condition, the formation energy of Bi_{Ag} is significantly higher, so the Fermi level is shifted closer to the valence band maximum. From this calculation result, we can see that i) Bi_{Ag} antisite defects are the predominant defect leading to the n-type conduction type of undoped $AgBiSe_2$ and ii) excess Se conditions (Se-rich environment) increase the formation energy of Bi_{Ag} to decrease the electron concentration. In fact, the presence of Bi_{Ag} in trigonal $AgBiSe_2$ was detected by the X-ray refinement study of Böcher et al. which means that the overall n-type properties of $AgBiSe_2$-based materials could be due to Bi_{Ag} antisites (Fig. 7f) [89]. Furthermore, the recent Hall measurement study on stoichiometric trigonal-phase $AgBiSe_2$ single crystal revealed its p-type conduction property, suggesting that the slow crystallization of $AgBiSe_2$ could reduce Bi_{Ag} concentration and the remaining V_{Ag} could be responsible for the p-type conductivity (Fig. 7g) [119]. Similarly, the n-to-p-type transition by excess Se precursor in $AgBiSe_2$ could also be reasonably understood by the suppressed formation of Bi_{Ag} as well (Fig. 7h).

3. Summary and outlook

We have reviewed the recent progress of $AgBiSe_2$ as a prospective TE material with high-performance capabilities in terms of lone-pair electron physics, spontaneous nanostructures, doping strategies, and thermal properties. While a number of research on TE materials is focused on reducing the lattice thermal conductivity, an intrinsically low lattice thermal conductivity of $AgBiSe_2$ provides a room to focus on enhancing the electrical properties. Carrier concentration tuning by aliovalent element doping or inducing band nestification have been introduced as feasible ways to improve electrical properties of $AgBiSe_2$. In addition, the temperature-dependent polymorphic property of trigonal $AgBiSe_2$ can be modulated by entropy engineering via alloying other endmembers such as GeSe, SnSe, and PbSe. Since the zT values of $AgBiSe_2$ are typically high at above 700 K, the $AgBiSe_2$-based high-temperature TE device would experience significant volume change during the operation due to polymorphic phase transformation, which is a major concern for the operational stability and overall performance of the $AgBiSe_2$-based TE device. Therefore, it is imperative to design room-temperature stable cubic $AgBiSe_2$ with high zT values. In addition, metallization and contact resistance, and thermal expansion coefficient mismatch between electrodes and $AgBiSe_2$ should be considered.

There are several unresolved issues from material aspect that should be investigated to understand the properties of $AgBiSe_2$ for practical applications. First, although Se vapor annealing has been introduced to stabilize the p-type conduction property of $AgBiSe_2$-based alloys, prolonged operation of $AgBiSe_2$ at high temperatures would cause a loss of Se due to its high volatility. Therefore, the intrinsic stability of $AgBiSe_2$ should be improved for fabricating stable TE modules. To achieve this goal. Finding suitable dopants to increase the stability of Se in the $AgBiSe_2$ lattice could be considered (e.g., improved chemical stability of copper selenides by indium doping [120]). One can also design a composition that can significantly suppress the formation of donor-like antisite defects. For example, p-type conductivity has been observed in $AgBiSe_2$–$AgSbSe_2$ alloys, presumably due to the prevention of donor-like Bi_{Ag} antisite defects and the formation of acceptor-like V_{Ag} defects [83]. Although the property of these systems has not yet been stabilized, this observation suggests that the intrinsic conductivity type can be controlled through the use of defect engineering. Second, a comprehensive characterization of the ordering and disordering of $AgBiSe_2$ should be performed. The electrical properties of cubic $AgBiSe_2$ change significantly before and after cation ordering and disordering; however, there are only few reports investigating the structural properties of ordered $AgBiSe_2$. In situ spectroscopic measurements could be helpful to understand the high-temperature

structural properties. Finally, a computational technique to simulate complex structure of cubic $AgBiSe_2$ should be developed to understand the defect chemistry and electronic band structure of pure and doped cubic $AgBiSe_2$. Currently, the effect of dopants in cubic $AgBiSe_2$ is calculated using an SQS cell [64,101]. However, SQS is designed to mimic disordered alloys, while cubic $AgBiSe_2$ has some degree of cation ordering. Therefore, in combination with experimentally measured structural information, a structural model should be developed to describe the real crystal structure of cubic $AgBiSe_2$.

The zT value of $AgBiSe_2$ is still about 1 at 773 K, which is much lower compared to other state-of-the-art TE materials [65,74]. However, several known strategies such as band convergence [121,122], lattice softening [123,124], and grain boundary engineering [125,126] have yet to be applied to $AgBiSe_2$-based TE materials, which can further improve the zT value. This would lead to the development of environmentally benign Pb-free TE devices with high performance capabilities for sustainable technologies.

Data availability

Data will be made available on request.

CRediT authorship contribution statement

Hanhwi Jang: Writing – original draft, Writing – review & editing. **Yeon Sik Jung:** Supervision. **Min-Wook Oh:** Supervision, Writing – original draft, Writing – review & editing.

Declaration of competing interest

The authors declare that they have no known competing financial interests or personal relationships that could have appeared to influence the work reported in this paper.

Acknowledgements

This work was supported by the National Research Foundation of the Republic of Korea (NRF) funded by the Ministry of Science and ICT (2021M2D1A1039966).

Appendix A. Supplementary data

Supplementary data to this article can be found online at https://doi.org/10.1016/j.heliyon.2023.e21117.

References

[1] P. Erickson, M. Lazarus, G. Piggot, Limiting fossil fuel production as the next big step in climate policy, Nat. Clim. Change 8 (12) (2018) 1037–1043.
[2] J. Yoon, et al., Heat-fueled enzymatic cascade for selective oxyfunctionalization of hydrocarbons, Nat. Commun. 13 (1) (2022) 3741.
[3] C. Forman, et al., Estimating the global waste heat potential, Renew. Sustain. Energy Rev. 57 (2016) 1568–1579.
[4] J. Mao, G. Chen, Z. Ren, Thermoelectric cooling materials, Nat. Mater. 20 (4) (2021) 454–461.
[5] Q. Yan, M.G. Kanatzidis, High-performance thermoelectrics and challenges for practical devices, Nat. Mater. 21 (5) (2022) 503–513.
[6] G. Tan, L.D. Zhao, M.G. Kanatzidis, Rationally designing high-performance bulk thermoelectric materials, Chem. Rev. 116 (19) (2016) 12123–12149.
[7] G.J. Snyder, E.S. Toberer, Complex thermoelectric materials, Nat. Mater. 7 (2) (2008) 105–114.
[8] J. He, T.M. Tritt, Advances in thermoelectric materials research: looking back and moving forward, Science 357 (6358) (2017), eaak9997.
[9] S. Abbey, et al., Twisted grain boundary leads to high thermoelectric performance in tellurium crystals, Energy Environ. Sci. 16 (2023) 125–137.
[10] S.I. Kim, et al., Dense dislocation arrays embedded in grain boundaries for high-performance bulk thermoelectrics, Science 348 (6230) (2015) 109–114.
[11] Y. Pei, H. Wang, G.J. Snyder, Band engineering of thermoelectric materials, Adv. Mater. 24 (46) (2012) 6125–6135.
[12] Y. Pei, et al., Convergence of electronic bands for high performance bulk thermoelectrics, Nature 473 (7345) (2011) 66–69.
[13] J.-H. Son, et al., Optimization of thermoelectric properties of n-type Bi2(Te,Se)3 with optimizing ball milling time, Rare Met. 37 (4) (2018) 351–359.
[14] T. Zhu, et al., Compromise and synergy in high-efficiency thermoelectric materials, Adv. Mater. 29 (14) (2017), 1605884.
[15] H. Ohta, et al., High thermoelectric power factor of high-mobility 2D electron gas, Adv. Sci. 5 (1) (2018), 1700696.
[16] L.W. Fu, et al., Hidden role of intrinsic Sb-rich nano-precipitates for high-performance Bi2-xSbxTe3 thermoelectric alloys, Acta Mater. 215 (2021), 117058.
[17] B. Zhu, et al., Realizing record high performance in n-type Bi2Te3-based thermoelectric materials, Energy Environ. Sci. 13 (7) (2020) 2106–2114.
[18] S.H. Park, et al., Fe-Ni-Cr diffusion barrier for high-temperature operation of Bi2Te3, J. Alloys Compd. 932 (2023), 167537.
[19] Y. Tang, et al., Convergence of multi-valley bands as the electronic origin of high thermoelectric performance in CoSb3 skutterudites, Nat. Mater. 14 (12) (2015) 1223–1228.
[20] Y. Tang, et al., Solubility design leading to high figure of merit in low-cost Ce-CoSb3 skutterudites, Nat. Commun. 6 (1) (2015) 7584.
[21] J. Gainza, et al., Unveiling the correlation between the crystalline structure of M-filled CoSb3 (M = Y, K, Sr) skutterudites and their thermoelectric transport properties, Adv. Funct. Mater. 30 (36) (2020), 2001651.
[22] H. Jang, et al., Fabrication of skutterudite-based tubular thermoelectric generator, Energies 13 (5) (2020) 1106.
[23] L.D. Zhao, et al., Ultralow thermal conductivity and high thermoelectric figure of merit in SnSe crystals, Nature 508 (7496) (2014) 373–377.
[24] C. Chang, et al., 3D charge and 2D phonon transports leading to high out-of-plane ZT in n-type SnSe crystals, Science 360 (6390) (2018) 778–783.
[25] A.T. Duong, et al., Achieving ZT=2.2 with Bi-doped n-type SnSe single crystals, Nat. Commun. 7 (1) (2016), 13713.
[26] S.H. Heo, et al., Solution-processed hole-doped SnSe thermoelectric thin-film devices for low-temperature power generation, ACS Energy Lett. 7 (6) (2022) 2092–2101.
[27] K.L. Peng, et al., Broad temperature plateau for high ZTs in heavily doped p-type SnSe single crystals, Energy Environ. Sci. 9 (2) (2016) 454–460.

[28] M.H. Lee, et al., Grain growth mechanism and thermoelectric properties of hot press and spark plasma sintered Na-doped PbTe, J. Alloys Compd. 786 (2019) 515–522.
[29] H. Jang, et al., Regulating Te vacancies through dopant balancing via excess Ag enables rebounding power factor and high thermoelectric performance in p-type PbTe, Adv. Sci. 8 (20) (2021), e2100895.
[30] B. Ryu, et al., Defects responsible for abnormal n-type conductivity in Ag-excess doped PbTe thermoelectrics, J. Appl. Phys. 118 (1) (2015), 015705.
[31] P. Jood, et al., Na doping in PbTe: solubility, band convergence, phase boundary mapping, and thermoelectric properties, J. Am. Chem. Soc. 142 (36) (2020) 15464–15475.
[32] K. Biswas, et al., High-performance bulk thermoelectrics with all-scale hierarchical architectures, Nature 489 (7416) (2012) 414–418.
[33] S. Ohno, et al., Phase boundary mapping to obtain n-type Mg3Sb2-based thermoelectrics, Joule 2 (1) (2018) 141–154.
[34] M. Wood, et al., Improvement of low-temperature zT in a Mg(3) Sb(2) -Mg(3) Bi(2) solid solution via Mg-vapor annealing, Adv. Mater. 31 (35) (2019), e1902337.
[35] K. Imasato, S.D. Kang, G.J. Snyder, Exceptional thermoelectric performance in Mg3Sb0.6Bi1.4 for low-grade waste heat recovery, Energy Environ. Sci. 12 (3) (2019) 965–971.
[36] J. Mao, et al., Defect engineering for realizing high thermoelectric performance in n-type Mg3Sb2-based materials, ACS Energy Lett. 2 (10) (2017) 2245–2250.
[37] J. Zhang, et al., Discovery of high-performance low-cost n-type Mg(3)Sb(2)-based thermoelectric materials with multi-valley conduction bands, Nat. Commun. 8 (1) (2017), 13901.
[38] S. Roychowdhury, et al., Enhanced atomic ordering leads to high thermoelectric performance in AgSbTe(2), Science 371 (6530) (2021) 722–727.
[39] J.K. Lee, et al., Effect of microstructure on thermoelectric conversion efficiency in metastable δ-phase AgSbTe2, Acta Mater. 222 (2022), 117443.
[40] K.F. Hsu, et al., Cubic AgPbmSbTe2+m: bulk thermoelectric materials with high figure of merit, Science 303 (5659) (2004) 818–821.
[41] Y. Yu, et al., Tunable quantum gaps to decouple carrier and phonon transport leading to high-performance thermoelectrics, Nat. Commun. 13 (1) (2022) 5612.
[42] H.S. Lee, et al., Herringbone structure in GeTe-based thermoelectric materials, Acta Mater. 91 (2015) 83–90.
[43] J.F. Dong, et al., Medium-temperature thermoelectric GeTe: vacancy suppression and band structure engineering leading to high performance, Energy Environ. Sci. 12 (4) (2019) 1396–1403.
[44] D. Liu, et al., Lattice plainification advances highly effective SnSe crystalline thermoelectrics, Science 380 (6647) (2023) 841–846.
[45] X. Zhang, et al., GeTe thermoelectrics, Joule 4 (5) (2020) 986–1003.
[46] C.L. Chen, et al., Thermoelectric properties of p-type polycrystalline SnSe doped with Ag, J. Mater. Chem. A 2 (29) (2014) 11171–11176.
[47] D.T. Morelli, V. Jovovic, J.P. Heremans, Intrinsically minimal thermal conductivity in cubic I-V-VI2 semiconductors, Phys. Rev. Lett. 101 (3) (2008), 035901.
[48] M. Dutta, et al., Local symmetry breaking suppresses thermal conductivity in crystalline solids, Angew. Chem. Int. Ed. 61 (15) (2022), e202200071.
[49] J. Ma, et al., Glass-like phonon scattering from a spontaneous nanostructure in AgSbTe2, Nat. Nanotechnol. 8 (6) (2013) 445–451.
[50] H. Jang, et al., Order-disorder transition-induced band nestification in AgBiSe2-CuBiSe2 solid solutions for superior thermoelectric performance, J. Mater. Chem. A 9 (8) (2021) 4648–4657.
[51] E.J. Skoug, D.T. Morelli, Role of lone-pair electrons in producing minimum thermal conductivity in nitrogen-group chalcogenide compounds, Phys. Rev. Lett. 107 (23) (2011), 235901.
[52] S. Geller, J. Wernick, Ternary semiconducting compounds with sodium chloride-like structure: AgSbSe2, AgSbTe2, AgBiS2, AgBiSe2, Acta Crystallogr. 12 (1) (1959) 46–54.
[53] M. Banas, J. Ottemann, Bohdanowiczite–nowy naturalny selenek srebra i bizmutu z Kletna w Sudetach, Przeglad Geol. 15 (1967), 240-240.
[54] C. Xiao, et al., High thermoelectric and reversible p-n-p conduction type switching integrated in dimetal chalcogenide, J. Am. Chem. Soc. 134 (44) (2012) 18460–18466.
[55] K. Hoang, et al., Atomic ordering and gap formation in Ag-Sb-based ternary chalcogenides, Phys. Rev. Lett. 99 (15) (2007), 156403.
[56] E. Quarez, et al., Nanostructuring, compositional fluctuations, and atomic ordering in the thermoelectric materials AgPb(m)SbTe(2+m). The myth of solid solutions, J. Am. Chem. Soc. 127 (25) (2005) 9177–9190.
[57] C. Manolikas, J. Spyridelis, Electron-microscopic study of polymorphism and defects in Agbise2 and Agbis2, Mater. Res. Bull. 12 (9) (1977) 907–913.
[58] J.L. Niedziela, et al., Controlling phonon lifetimes via sublattice disordering in AgBiSe2, Phys. Rev. Mater. 4 (10) (2020), 105402.
[59] H. Jang, et al., Suppressing charged cation antisites via Se vapor annealing enables p-type dopability in AgBiSe(2) -SnSe thermoelectrics, Adv. Mater. 34 (38) (2022), e2204132.
[60] S. Baroni, R. Resta, Ab initio calculation of the low-frequency Raman cross section in silicon, Phys. Rev. B 33 (8) (1986) 5969–5971.
[61] R. Chen, et al., Entropy-driven multiscale defects enhance the thermoelectric properties of ZrCoSb-based half-Heusler alloys, Chem. Eng. J. (2022), 140676.
[62] A. Zunger, et al., Special quasirandom structures, Phys. Rev. Lett. 65 (3) (1990) 353–356.
[63] X. Chen, et al., Direct observation of chemical short-range order in a medium-entropy alloy, Nature 592 (7856) (2021) 712–716.
[64] H. Jang, et al., Suppressing charged cation antisites via Se vapor annealing enables p-type dopability in AgBiSe2–SnSe thermoelectrics, Adv. Mater. 34 (38) (2022), 2204132.
[65] L. Pan, D. Berardan, N. Dragoe, High thermoelectric properties of n-type AgBiSe2, J. Am. Chem. Soc. 135 (13) (2013) 4914–4917.
[66] M. Zou, et al., Comparing the role of annealing on the transport properties of polymorphous AgBiSe(2) and monophase AgSbSe(2), RSC Adv. 8 (13) (2018) 7055–7061.
[67] D.T. Morelli, J.P. Heremans, Thermal conductivity of germanium, silicon, and carbon nitrides, Appl. Phys. Lett. 81 (27) (2002) 5126–5128.
[68] M.T. Agne, R. Hanus, G.J. Snyder, Minimum thermal conductivity in the context of diffuson-mediated thermal transport, Energy Environ. Sci. 11 (3) (2018) 609–616.
[69] J.K. Lee, et al., Enhanced thermoelectric properties of AgSbTe(2) obtained by controlling heterophases with Ce doping, Sci. Rep. 7 (1) (2017) 4496.
[70] Y.B. Luo, et al., High-performance thermoelectrics from cellular nanostructured Sb2Si2Te6, Joule 4 (1) (2020) 159–175.
[71] H. Jang, et al., Comparative study of thermoelectric properties of Sb(2)Si(2)Te(6) and Bi(2)Si(2)Te(6), ACS Appl. Mater. Interfaces 14 (1) (2022) 1270–1279.
[72] G. Tan, et al., High thermoelectric performance of p-type SnTe via a synergistic band engineering and nanostructuring approach, J. Am. Chem. Soc. 136 (19) (2014) 7006–7017.
[73] Y. Chen, et al., SnTe-AgSbTe2 thermoelectric alloys, Adv. Energy Mater. 2 (1) (2012) 58–62.
[74] S.N. Guin, V. Srihari, K. Biswas, Promising thermoelectric performance in n-type AgBiSe2: effect of aliovalent anion doping, J. Mater. Chem. A 3 (2) (2015) 648–655.
[75] R.D. Shannon, Revised effective ionic-radii and systematic studies of interatomic distances in halides and chalcogenides, Acta Crystallogr. A 32 (Sep1) (1976) 751–767.
[76] C. Tantardini, A.R. Oganov, Thermochemical electronegativities of the elements, Nat. Commun. 12 (1) (2021) 2087.
[77] Q.R. Xia, et al., Chemical composition engineering leading to the significant improvement in the thermoelectric performance of AgBiSe2-based n-type solid solutions, ACS Appl. Energy Mater. 4 (3) (2021) 2899–2907.
[78] X.C. Liu, D. Jin, X. Liang, Enhanced thermoelectric performance of n-type transformable AgBiSe2 polymorphs by indium doping, Appl. Phys. Lett. 109 (13) (2016), 133901.
[79] Y.D. Guan, et al., Enhanced thermoelectric performance realized in AgBiS2 composited AgBiSe2 through indium doping and mechanical alloying, Appl. Phys. Lett. 112 (21) (2018), 213905.
[80] S. Li, et al., Defect engineering for realizing p-type AgBiSe2 with a promising thermoelectric performance, Chem. Mater. 32 (8) (2020) 3528–3536.
[81] D.S. Parker, A.F. May, D.J. Singh, Benefits of carrier-pocket anisotropy to thermoelectric performance: the case of p-type AgBiSe2, Phys. Rev. Appl. 3 (6) (2015), 064003.
[82] S.N. Guin, et al., High thermoelectric performance in tellurium free p-type AgSbSe2, Energy Environ. Sci. 6 (9) (2013) 2603–2608.
[83] T. Bernges, et al., Local structure and influence of Sb substitution on the structure-transport properties in AgBiSe(2), Inorg. Chem. 58 (14) (2019) 9236–9245.

[84] K. Sudo, et al., Doping-Induced polymorph and carrier polarity changes in thermoelectric Ag(Bi,Sb)Se2 solid solution, Inorg. Chem. 58 (11) (2019) 7628–7633.
[85] S. Lin, et al., Tellurium as a high-performance elemental thermoelectric, Nat. Commun. 7 (1) (2016), 10287.
[86] J. Park, et al., When band convergence is not beneficial for thermoelectrics, Nat. Commun. 12 (1) (2021) 3425.
[87] K. Imasato, et al., Band engineering in Mg3Sb2 by alloying with Mg3Bi2 for enhanced thermoelectric performance, Mater. Horiz. 5 (1) (2018) 59–64.
[88] Y. Goto, et al., Effect of Te substitution on crystal structure and transport properties of AgBiSe(2) thermoelectric material, Dalton Trans. 47 (8) (2018) 2575–2580.
[89] F. Bocher, et al., Vacancy and anti-site disorder scattering in AgBiSe(2) thermoelectrics, Dalton Trans. 46 (12) (2017) 3906–3914.
[90] H.J. Wu, et al., Ultralow thermal conductivity in n-type Ge-doped AgBiSe2 thermoelectric materials, Acta Mater. 141 (2017) 217–229.
[91] X.-C. Liu, M.-Y. Pan, Structural phase transition and related thermoelectric properties in Sn doped AgBiSe2, Crystals 11 (2021), https://doi.org/10.3390/cryst11091016.
[92] Y. Luo, et al., High thermoelectric performance in the new cubic semiconductor AgSnSbSe(3) by high-entropy engineering, J. Am. Chem. Soc. 142 (35) (2020) 15187–15198.
[93] B. Jiang, et al., High-entropy-stabilized chalcogenides with high thermoelectric performance, Science 371 (6531) (2021) 830–834.
[94] Y.T. Qiu, et al., Realizing high thermoelectric performance in GeTe through decreasing the phase transition temperature via entropy engineering, J. Mater. Chem. A 7 (46) (2019) 26393–26401.
[95] R. Chen, et al., Significantly optimized thermoelectric properties in high-symmetry cubic Cu7PSe6 compounds via entropy engineering, J. Mater. Chem. A 6 (15) (2018) 6493–6502.
[96] S. Zhi, et al., Medium entropy-enabled high performance cubic GeTe thermoelectrics, Adv. Sci. 8 (12) (2021), 2100220.
[97] C. Yang, et al., Synergistic optimization of the electronic and phonon transports of N-type argyrodite Ag(8)Sn(1-x)Ga(x)Se(6) (x = 0-0.6) through entropy engineering, ACS Appl. Mater. Interfaces 13 (47) (2021) 56329–56336.
[98] G. Liang, et al., (GeTe)(1-x)(AgSnSe(2))(x): strong atomic disorder-induced high thermoelectric performance near the ioffe-regel limit, ACS Appl. Mater. Interfaces 13 (39) (2021) 47081–47089.
[99] S. Roychowdhury, et al., Stabilizing n-type cubic GeSe by entropy-driven alloying of AgBiSe(2) : ultralow thermal conductivity and promising thermoelectric performance, Angew. Chem. Int. Ed. 57 (46) (2018) 15167–15171.
[100] M. Samanta, et al., Realization of both n- and p-type GeTe thermoelectrics: electronic structure modulation by AgBiSe(2) alloying, J. Am. Chem. Soc. 141 (49) (2019) 19505–19512.
[101] S. Chandra, et al., Modulation of the electronic structure and thermoelectric properties of orthorhombic and cubic SnSe by AgBiSe(2) alloying, Chem. Sci. 12 (39) (2021) 13074–13082.
[102] H.X. Wang, et al., Crystal structure modulation of SnSe thermoelectric material by AgBiSe2 solid solution, J. Eur. Ceram. 43 (8) (2023) 3383–3389.
[103] S. Li, et al., Manipulation of phase structure and Se vacancy to enhance the average thermoelectric performance of AgBiSe2, Mat. Today Phys. 27 (2022), 100837.
[104] M. Dutta, et al., Bonding heterogeneity and lone pair induced anharmonicity resulted in ultralow thermal conductivity and promising thermoelectric properties in n-type AgPbBiSe(3), Chem. Sci. 10 (18) (2019) 4905–4913.
[105] H. Zhu, et al., Entropy engineered cubic n-type AgBiSe2 alloy with high thermoelectric performance in fully extended operating temperature range, Adv. Energy Mater. 11 (5) (2020), 2003304.
[106] L. Zhang, et al., Stabilizing n-type cubic AgBiSe2 thermoelectric materials through alloying with PbS, J. Materiomics (2023).
[107] H. Zhu, et al., Manipulating lattice distortion to promote average thermoelectric power factor in metavalently bonded AgBiSe2, Acta Mater. 259 (2023), 119260.
[108] T. Zhao, et al., High thermoelectric performance of tellurium-free n-type AgBi1-xSbxSe2 with stable cubic structure enabled by entropy engineering, Acta Mater. 220 (2021), 117291.
[109] B. Mukherjee, et al., NIR Schottky photodetectors based on individual single-crystalline GeSe nanosheet, ACS Appl. Mater. Interfaces 5 (19) (2013) 9594–9604.
[110] T. Lyu, et al., Stepwise Ge vacancy manipulation enhances the thermoelectric performance of cubic GeSe, Chem. Eng. J. 442 (2022), 136332.
[111] M.D. Nielsen, V. Ozolins, J.P. Heremans, Lone pair electrons minimize lattice thermal conductivity, Energy Environ. Sci. 6 (2) (2013) 570–578.
[112] Z.H. Liu, et al., A material catalogue with glass-like thermal conductivity mediated by crystallographic occupancy for thermoelectric application, Energy Environ. Sci. 14 (6) (2021) 3579–3587.
[113] E.S. Bozin, et al., Entropically stabilized local dipole formation in lead chalcogenides, Science 330 (6011) (2010) 1660–1663.
[114] A. Banik, et al., Engineering ferroelectric instability to achieve ultralow thermal conductivity and high thermoelectric performance in Sn1-xGexTe, Energy Environ. Sci. 12 (2) (2019) 589–595.
[115] M. Dutta, et al., Emphanisis in cubic (SnSe)0.5(AgSbSe2)0.5: dynamical off-centering of anion leads to low thermal conductivity and high thermoelectric performance, J. Am. Chem. Soc. 143 (40) (2021) 16839–16848.
[116] S.J. Billinge, M.G. Kanatzidis, Beyond crystallography: the study of disorder, nanocrystallinity and crystallographically challenged materials with pair distribution functions, Chem. Commun. (7) (2004) 749–760.
[117] T. Proffen, et al., Structural analysis of complex materials using the atomic pair distribution function - a practical guide, Z. Kristallogr. 218 (2) (2003) 132–143.
[118] J. Male, et al., The importance of phase equilibrium for doping efficiency: iodine doped PbTe, Mater. Horiz. 6 (7) (2019) 1444–1453.
[119] M. William Carry, et al., Fermi energy-level shift of p-type AgBiSe2 single crystal featuring semiconductor-to-metal transition at cryogenics, Semicond. Sci. Technol. 37 (6) (2022), 065023.
[120] A.A. Olvera, et al., Partial indium solubility induces chemical stability and colossal thermoelectric figure of merit in Cu2Se, Energy Environ. Sci. 10 (7) (2017) 1668–1676.
[121] A. Banik, et al., High power factor and enhanced thermoelectric performance of SnTe-AgInTe2: synergistic effect of resonance level and valence band convergence, J. Am. Chem. Soc. 138 (39) (2016) 13068–13075.
[122] W. Liu, et al., Convergence of conduction bands as a means of enhancing thermoelectric performance of n-type Mg2Si(1-x)Snx solid solutions, Phys. Rev. Lett. 108 (16) (2012), 166601.
[123] R. Hanus, et al., Lattice softening significantly reduces thermal conductivity and leads to high thermoelectric efficiency, Adv. Mater. 31 (21) (2019), 1900108.
[124] T.J. Slade, et al., Charge-carrier-mediated lattice softening contributes to high zT in thermoelectric semiconductors, Joule 5 (5) (2021) 1168–1182.
[125] T. Luo, et al., Nb-mediated grain growth and grain-boundary engineering in Mg3Sb2-based thermoelectric materials, Adv. Funct. Mater. 31 (28) (2021), 2100258.
[126] Y. Lin, et al., Expression of interfacial Seebeck coefficient through grain boundary engineering with multi-layer graphene nanoplatelets, Energy Environ. Sci. 13 (11) (2020) 4114–4121.